Induced mixing in stratified fluids by rising bubbles in a thin gap

Maathangi Ganesh, Sangkyu Kim, and Sadegh Dabiri

Induced mixing in stratified fluids by rising bubbles in a thin gap

[1] Maathangi Ganesh, [1] Sangkyu Kim, and [1] Sadegh Dabiri†

[1]Purdue University, West Lafayette, Indiana, 47907

This work reports a numerical study of mixing in temperature or density stratified fluids induced by the motion of a mono-dispersed swarm of bubbles in a thin gap. Simulations are run for void fractions between 3.35% and 13.4%. The strength of stratification is varied by changing the Froude number between 4.5 and 12.74. The confinement prevents turbulence production, and mixing occurs primarily due to transport of colder liquid into the hotter layers by the bubble wake. Bubbles move in a zigzag motion attributed to the periodic vortex shedding in their wake. We report the formation of horizontal clusters and establish a direct correlation between the size of clusters and the rise velocity of the bubbles. We report an increase in the buoyancy flux across the isopycnals as the void fraction increases. The fraction of energy production due to the buoyancy flux increases with the strength of stratification, giving rise to a higher mixing efficiency. At the same time, cross isopycnal diffusion is higher at weaker stratification strengths.

Key words:

1. Introduction

Multiple studies have been carried out on the dynamics of bubbles in unconfined environments in both homogeneous (Bunner & Tryggvason (2002*a*), Bunner & Tryggvason (2002*b*), Riboux *et al.* (2010)) and stratified background fluids (Dabiri *et al.* (2015), Bayareh *et al.* (2016), Díaz-Damacillo *et al.* (2016), Ardekani *et al.* (2017)). A summary of previous works done on quantifying agitation and mixing due to bubble motion is presented by Risso (2018).

Recently, more works have been focused on the motion of bubbles in confined Hele-Shaw cells. Confinement of bubbles alters the bubble dynamics. There is a thin liquid film between the bubble and the wall. The bubble wake is subjected to shear stress at the wall, and the wake length is of the order a few bubble diameters, which is less than in unbounded flows. Mixing in the background liquid can occur either due to the transport by the bubble wake or due to turbulent dispersion (Alméras *et al.* (2015)). In a configuration where the bubbles are confined in a thin gap, turbulence cannot occur even at high Reynolds numbers (Re) since the vortices have a short lifetime (Bouche *et al.* (2013), Bouche *et al.* (2014)). A flattened bubble has a much larger interfacial area, and hence effective diameter, for a given bubble volume in comparison to an unconfined bubble. Thus, the mixing in the background fluid is mainly caused by the bubble wakes, despite large Reynolds numbers. Bush & Eames (1998) showed through experimental and analytical studies that the primary wake advects fluid with the bubble generating an

---

† Email address for correspondence: dabiri@purdue.edu

enhanced reflux and promoting longitudinal dispersion. They chose the confined geometry since the effects of drift and reflux are more pronounced in two dimensions with simpler flow visualization. Alméras *et al.* (2015) experimentally studied the transport and mixing of low-diffusivity dye in a homogeneous swarm of bubbles. They observed that at low void fractions, α, the diffusion coefficient scales as $\alpha^{0.4}$ in unconfined flows. They established that in confined flows, mixing could not be modeled as a diffusion process since it occurs due to the transport by bubble wakes. Bouche *et al.* (2013) also conducted experiments to study the mixing of a passive scalar with a low diffusivity in a swarm of bubbles. It was shown that mixing is enhanced in the confined geometry due to the dominant role of the bubble wake in the scalar transport. The Fickian law of diffusion cannot reproduce the mixing since the temporal evolution of the dye concentration in the observation window was seen to decay exponentially.

The differences in confined and unconfined bubbly flows can further be characterized by looking at the rise velocity and velocity fluctuations of the bubbles. It was shown through experiments that for high Reynolds number bubbles rising in a Hele-Shaw cell, the drag coefficient is constant for a wide range of Reynolds numbers, in contrast to the unconfined case (Roig *et al.* 2012). The vorticity is attenuated due to the confinement. The combined numerical and experimental studies by Wang *et al.* (2016) showed that with an increase in the gap width, the drag coefficient decreases accompanied by an increase in the bubble terminal velocity. They also showed that as the gap width is increased, the wake length becomes larger. Study of rising motion of bubbles near a vertical wall (Dabiri & Bhuvankar 2016) reported an increase in average rise velocity of bubbles with an increase in void fraction between 3.75% and 60% due to the formation of vertical clusters. It was further shown by Bouche *et al.* (2012) that in confined bubbly flows, velocity fluctuations are due to the disturbances localized near the bubbles, and scale as $\alpha^{0.46}$ in the vertical direction, while in the horizontal direction the fluctuations are mainly due to the vortex shedding. They also reported a slight increase in the vertical rise velocity with an increase in void fraction. This is in contrast with the unconfined case. Thus the classic hindrance effect used to explain the bubble rise velocity trend in the unconfined case is not valid here. The study of agitation in the liquid phase due to rising bubbles in a thin gap further confirms the fact that vertical fluctuations are governed by hydrodynamic interactions (Bouche *et al.* 2014). These fluctuations were attributed to the flow disturbances localized in the bubble vicinity.

The rising motion of bubbles and drops in a stably stratified fluid causes de-stratification and mixing of the density layers (Dabiri *et al.* (2015), Ardekani *et al.* (2017)). The bubble dynamics is also affected by the stratification. Bayareh *et al.* (2016) studied the dynamics of two drops in a density stratified fluid. They reported the suppression of horizontal and vertical motion for the side-by-side drop configuration. In-line drops are shown to retain their configuration, unlike the non-stratified case. The rise velocity and velocity fluctuation of a swarm of drops rising in a linearly stratified fluid are suppressed compared to the homogeneous case (Dabiri *et al.* (2015)). Dabiri *et al.* (2015) also reported enhanced horizontal cluster formation. Ardekani *et al.* (2017) reported a similar trend in their study of the motion of particles and drops in stratified fluids. Chen & Cardoso (2000) studied mixing induced in a two-layer density stratification by a bubble plume. They showed that small bubbles de-stratify the lower layer, while large bubbles increase the density of the upper layer. In the case of large bubbles rising through a stably-stratified sharp interface with a zigzag trajectory, it was seen that the drift volume detaches from the bubble, leaving a trail of heavier fluid in the lighter phase leading to enhanced mixing (Díaz-Damacillo *et al.* 2016). In the case of a bubble plume rising through a step density distribution, Baines & Leitch (1992) showed

that the liquid plume impinged on the interface and split. About 20% of the volume flux followed the bubbles into the upper layer, while the larger volume flux entrained the upper layer fluid and fell back onto the top of the lower layer, reducing stratification. They further demonstrated that, in the case of a linear density distribution, three distinct layers are formed. The top and bottom layers are similar to those formed in the step density distribution, while the middle layer preserves the linear stratification. This middle layer reduces in length and ultimately vanishes, leading to the step density configuration. Neto *et al.* (2016) conducted similar experiments where a bubble plume rising through the ambient fluid with two-layer stratification is negatively buoyant when the mixture reaches the top layer and forms a fountain. The speed of the bubbles exceeds the speed of the fountain due to which the lower layer of the fountain rises a finite distance in the upper layer entraining the upper layer fluid. After a finite time, the entrained liquid collapses, leading to an intermediate mixing layer. Blanchette (2013) used numerical simulations to describe the effects of settling particles on a temperature stratified fluid. It was seen that for the settling of a single particle, the time evolution of the height of an isopycnal shows a damped oscillatory motion with a period of the order of $1/N$, where N is the $Brunt - Väisälä$ frequency. As volume fraction of the particles increases, the stratification is disrupted, giving rise to a well-mixed fluid. Wang & Ardekani (2015) studied biogenic mixing of swimmers in stratified fluids. Mixing was quantified in terms of Cox number, diapycnal eddy diffusivity and mixing efficiency. Mixing characteristics were seen to increase with higher volume fractions and higher density stratification.

Despite the above-mentioned studies, the mixing of density stratified fluids due to bubble motion in a confined geometry is poorly understood. The study of confined bubbly flow has various applications. Confined bubbly flow is used in the cooling process in microelectronic devices (Wilmarth & Ishii 1994). Gas-liquid flow in narrow channels is also important in nuclear industries for cooling purposes (Spicka *et al.* 2001). Many heat exchangers and chemical reactors involve bubble columns (Bouche *et al.* 2014). Having a bubbly flow is useful in causing liquid agitation and consequently, liquid mixing without the need for any external mechanical power. The confined case is of importance because we are able to isolate the effects that bubble wake transport has on mixing. This would otherwise be impossible in an unconfined domain where mixing happens both due to transport by bubble wake as well as bubble induced turbulent fluctuations.

The level of mixing induced in the liquid and mixing time is also affected by the liquid stratification. Bubble plume mixers are used for destratification of temperature stratified lakes and reservoirs, in order to preserve freshwater. Bubble plumes are also used as bubble curtains for containment of oil spills in oceans (Asaeda & Imberger 1993). In the present numerical study, the effects of density stratification and confinement on the rising motion of bubbles have been tackled. An insight into various physical parameters that describes the flow has been presented, and the mixing induced by the bubble motion has been quantified. Path instability in the confined domain caused by periodic vortex shedding is observed and quantified. It is seen that as void fraction, α, increases, the buoyancy flux across the pycnolines increases. It is also shown that with an increase in the stratification strength, the fraction of total energy lost to buoyancy increases.

2. Problem Description

Our objective is to simulate the rising motion of air bubbles in a narrow gap between two rigid walls in a temperature stratified Newtonian fluid. The distance between the walls is comparable to the effective diameter of the bubbles. The two boundaries in
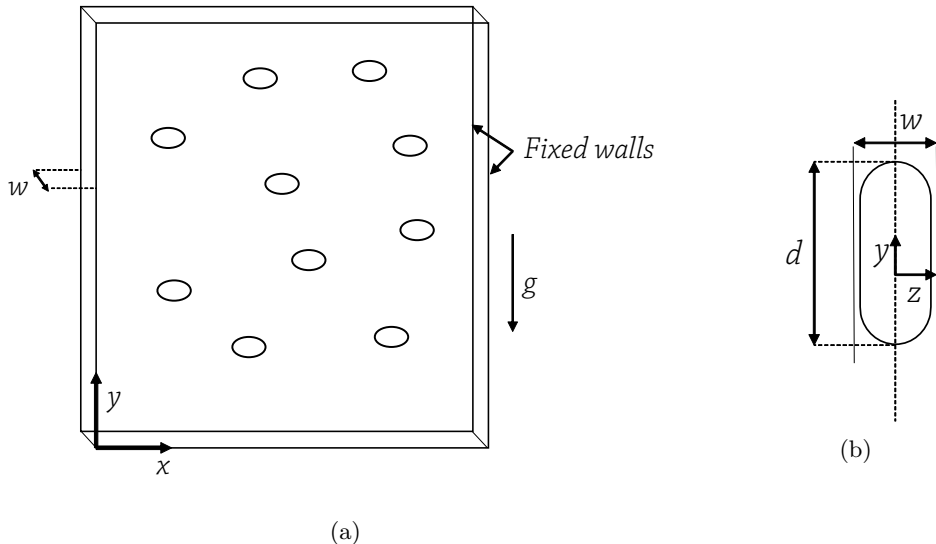
Figure 1: Schematic of the computational set-up (a) view of the bubbles rising in the domain (b) $y - z$ view of a single bubble which is confined between two solid walls

the z-direction are fixed (see figure 1a) and have no-slip velocity boundary conditions. The effective bubble diameter, d_{eff}, is dependent on the separation between the two fixed walls, w. In the present simulations, monodisperse distribution of bubbles with $w/d \approx 0.31$, where d is the initial effective bubble diameter, is maintained. A periodic velocity boundary condition is imposed in the x and y directions. Linear temperature stratification is initially imposed in the y-direction (vertical). T is the actual temperature which is given by $T = T_m + \frac{dT}{dy}y$, where $\frac{dT}{dy}$ is the constant background temperature gradient. The second term gives rise to a temperature field linearly varying in y. T_m is the temperature perturbation. Thus, in order to maintain the linear background stratification, a periodic boundary condition is implemented for the temperature perturbation, T_m. The temperature stratification leads to a linear density stratification. Even though we use temperature as the stratifying agent in our study, the analysis for concentration stratification is similar.

The bubbles are initialized with their z-centers at the midpoint between the two walls. Since the effective bubble diameter is much larger than the gap between the walls, the bubbles are initialized as ellipsoids. The effective two-dimensional diameter of the bubble is calculated as $d_{eff} = \sqrt{4A/\pi}$, where A is the projected area of the bubble in the $x - y$ plane. The given configuration leads to a free rise of bubbles under the effect of buoyancy. As the bubbles rise, they become flattened and confined (fig 1b) between the solid walls.

The dimensionless parameters used to characterize the motion of bubbles include the Archimedes number, $Ar = \rho_f \sqrt{gd}d/\mu_f$, Reynolds number, $Re_0 = \rho_f V_0 d/\mu_f$, Bond number, $Bo = \rho_f g d^2/\sigma$ and Weber number, $We = \rho_f V_0^2 d/\sigma$, which is the ratio of inertial to interfacial force. These four quantities are kept fixed throughout this study at $Re = 460$, $Ar = 807$, $Bo = 3.46$ and $We = 1.12$. These values essentially represent air bubbles of diameter 3.8mm in water. Here ρ_f and μ_f are the density and dynamic viscosity of the background fluid, d is the bubble diameter, g is the gravitational acceleration, σ is the interfacial tension and $V_0 = 0.57\sqrt{gd}$ is the mean rise velocity of an isolated bubble at $600 \leqslant Ar \leqslant 1500$ (Roig et $al.$ (2012), Bouche et $al.$ (2012)). The stratification of the background fluid can be characterized by the Froude number

$Fr = V_0/(Nd)$. Here N, the *Brunt-Väisälä* frequency, also known as the buoyancy frequency, is given by $N = (\beta g/\rho_0)^{1/2}$. In the expression for N, β is the vertical density gradient in the background fluid and ρ_0 is the background density without the stratification. The void fraction, α, of N_b number of bubbles in the domain is given by $\alpha = \frac{4}{3} N_b \pi abc/(LBw)$ where a, b and c are the axis lengths of the initially ellipsoidal bubble, w is the gap between the two walls while L and B are the length and breadth of the computational domain. Fr and α are varied in the simulations to achieve different levels of background stratification and different flow configurations. The density and viscosity ratios of the background fluid to the bubbles are maintained at $\rho_f/\rho_d = 100$ and $\mu_f/\mu_d = 10$.

Bubble dynamics is analyzed by studying the average velocity of bubbles at different void fractions and stratification strengths, which is quantified by the Froude number. Bubble dispersion and trajectories are studied. The autocorrelation function of horizontal bubble velocity gives interesting insights into the path and behavior of the bubbles. We also quantify the mixing which takes place in the background fluid, by computing mixing efficiency, diapycnal eddy diffusivity, and the Cox number.

3. Formulation and Numerical Implementation

The governing differential equations for the motion of a swarm of bubbles in a linear stratified fluid under the Boussinesq approximation are given by

$$\nabla \cdot \mathbf{u} = 0, \tag{3.1}$$

$$\rho_0 \frac{D\mathbf{u}}{Dt} = -\nabla p + (\rho - \bar{\rho})\mathbf{g} + \nabla \cdot \mu_f(\nabla \mathbf{u} + (\nabla \mathbf{u})^T) + \int \sigma k \mathbf{n} \delta(\mathbf{x} - \mathbf{x}')dA', \tag{3.2}$$

$$\frac{DT}{Dt} = \nabla \cdot (\kappa \nabla T), \tag{3.3}$$

where $\mathbf{u}$ is the velocity vector, p is the pressure field and $\mathbf{g}$ is the gravitational acceleration. ρ_0 is the background density without the stratification given by $\rho_0 = \phi \rho_f + (1 - \phi)\rho_d$, where ρ_f and ρ_d are the densities of the continuous and dispersed phase respectively. ρ is the actual physical density, which includes the linear stratification due to temperature given by $\rho = \rho_0(1 - \gamma(T - T_0))$, where γ is the coefficient of thermal expansion. $\bar{\rho}$ is the volumetric average density of the domain. $\bar{\rho}\mathbf{g}$ is subtracted from the body force so that the total force on the computational domain is zero, and the domain remains stationary with no net flow in the background liquid. ϕ is the marker function, which has a value 0 in the dispersed phase and 1 in the continuous phase. The last term in equation 3.2 accounts for the interfacial tension effects between the two phases. k, $\mathbf{n}$, and δ are twice the mean curvature of bubble interface, unit normal to the interface, and Dirac delta function, respectively. $\mathbf{x}'$ is a point on the interface, and dA' is the surface element at the interface. κ denotes the thermal diffusivity of the fluid. Initial values of all components of velocity and T_m, which is the temperature deviation from the linear field, are set to zero. Since the effective temperature is given by $T = T_m + \frac{dT}{dy}y$, a linear temperature exists in the domain initially.

A finite-volume/front tracking method (Unverdi & Tryggvason 1992) is used to solve the set of governing equations on a staggered grid. The projection method (Chorin (1968)) is used to enforce continuity. This gives rise to an explicit Poisson Equation for the pressure, which is solved using the HYPRE library (Falgout & Yang 2002).
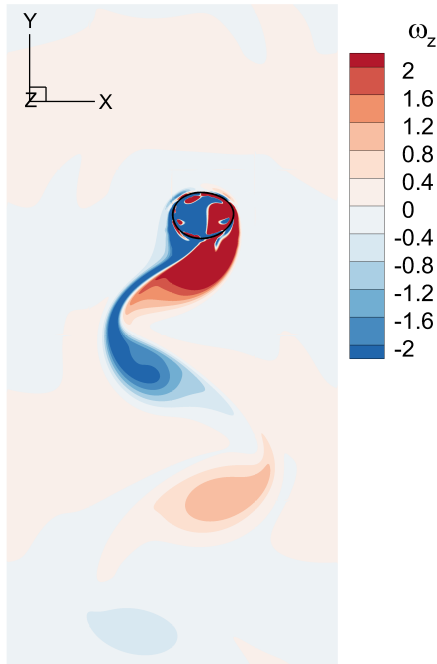
Figure 2: Contours of non-dimensional vorticity for a single bubble in computational domain at t=1.57s

The third order QUICK (Quadratic Upstream Interpolation for Convective Kinetics) (Leonard (1979)) scheme is used for the momentum convection terms, while the second-order central differencing scheme is used for diffusive terms. A second-order Runge-Kutta scheme is used for time advancement.

4. Results and Discussion

Simulations are run in a doubly periodic domain with a size of $5d \times 10d \times 0.31d$. 4.19 million grid points are used to resolve the flow, with 51 points across the bubble diameter initially. Void fractions of 3.35%, 8.37%, and 13.4% are used. The flow configuration represents air bubbles of diameter 3.8mm in water. Initial Reynolds number of $Re_0 = \frac{\rho_f(0.57\sqrt{gd})d}{\mu_f} \approx 460$ is used for all the simulations.

4.1. Domain size dependence

The computational domain size is tested for domain size dependency. The length of the domain in the vertical direction is the most important one due to the wake of the bubble. It must be made sure that any bubble does not interact with its own wake once it crosses the boundary of the periodic domain and re-enters on the other side. This implies that the length of the domain must be greater than the length of the wake. The length of the wake behind the bubble decreases as the void fraction increases due to the interaction between the bubbles (Bouche *et al.* (2014)). Thus looking at the wake for a single bubble is appropriate when testing for domain size dependency.

Simulations are run with a single bubble in the computational domain at an $\alpha = 0.84\%$ with $L_y = 10d$. The non-dimensional vorticity contours are plotted (figure 2). Non-dimensionalization is done by dividing vorticity by $v_{b,avg}/d$, where $v_{b,avg}$ is the average
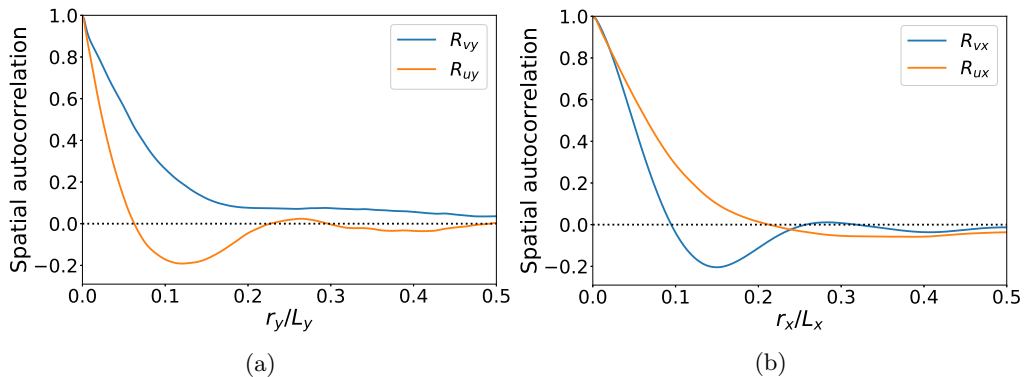
Figure 3: Spatial velocity correlation for the domain in the (a) Vertical direction (b) Horizontal direction for $\alpha = 13.4\%$

rise velocity of the bubbles. Periodic vortex shedding consisting of counter-rotating vortices can be seen behind the bubble. The vortices which are detached from behind the bubble die out rapidly. Simulations are also run with $L_y = 20d$, and the bubble Reynolds numbers in the vertical direction are compared. It was found that the difference in average Reynolds number between the two cases is 0.8%. Hence, $L_y = 10d$ is used for the rest of the results.

We further look at the spatial autocorrelations of both vertical (v) and horizontal (u) velocities with spacing in the vertical(r_y) (figure 3a) and horizontal(r_x) (figure 3b) directions for $\alpha = 13.4\%$. Both r_x and r_y have been non-dimensionalized by L_x and L_y, respectively, and the autocorrelation has been time-averaged after the flow has reached a statistically steady state. Figure 3 shows that as the spacing is increased both in the horizontal and vertical directions, the autocorrelation dies to 0 as r_x and r_y approach $L_x/2$ and $L_y/2$, respectively. Thus we can conclude that for the periodic boundaries, the domain size is sufficiently large.

4.2. Bubble trajectories

The dispersion of bubbles in the horizontal direction can be observed by superimposing the displacements of each bubble center with respect to its own location. Figure 4 shows that the dispersion increases with an increase in α. For a void fraction of 3.35%, a regular oscillation of bubbles about the center is seen. As α increases, the interactions between the bubbles also increase, and the motion of the bubbles becomes more chaotic, causing more dispersion.

The trajectories of bubbles at different void fractions are plotted in figure 5 to capture their zigzag motion. Kelley & Wu (1997) experimentally showed the zigzag motion of a bubble rising in a Hele-Shaw cell and established that it is due to the periodic vortex shedding. This was observed in our simulations, where the counter-rotating nature of the vortices is seen for the case of a single bubble (figure 2).

4.3. Flow field

Looking at the flow field around the bubbles gives interesting insights into their behavior. Figure 6a shows the flow field on the $y - x$ plane with a contour plot of vorticity at a particular time instant. As before, periodic vortex shedding can be observed. At this void fraction ($\alpha = 8.37\%$), the wake of the bubbles interact with each other causing the wake length to be even shorter than the single bubble case. Figure 6b shows the
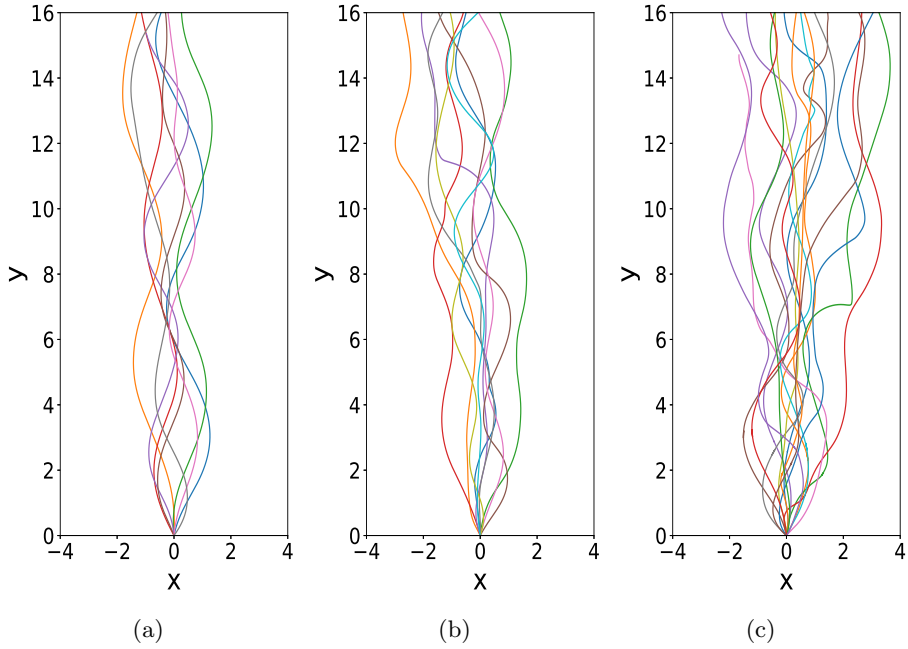
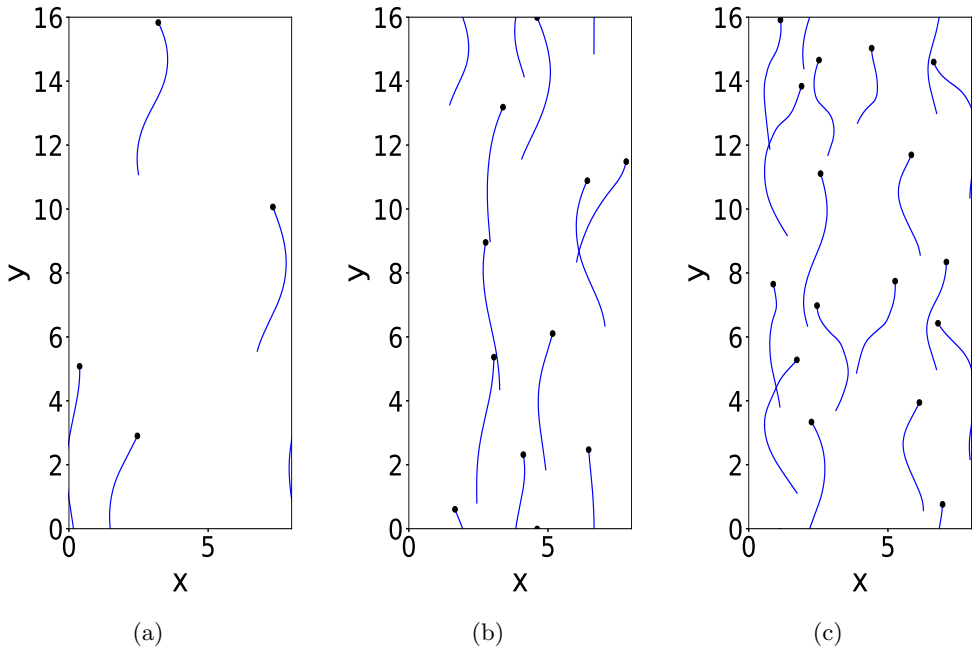Figure 4: Bubble center displacements for $\alpha =$ (a) 3.35%, (b) 8.37% and (c) 13.4% at $Fr = 6.37$

Figure 5: Bubble trajectories for $\alpha =$ (a) 3.35%, (b) 8.37% and (c) 13.4% at $Fr = 6.37$
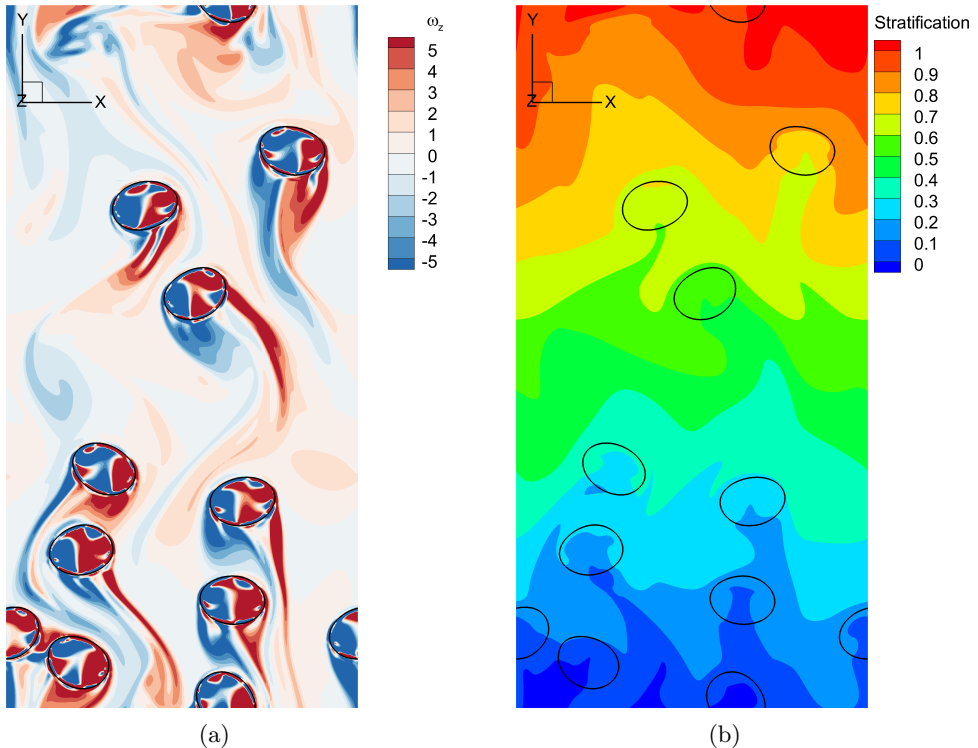
Figure 6: Flow field for $\alpha = 8.37\%$ at $Fr = 6.37$ (a) Non-dimensional z-vorticity contours (b) Temperature contours normalized by its highest value at t=0

temperature contours which are non-dimensionalized by the highest temperature value at t=0. The linearity of the temperature profile in the y-direction has been disrupted by the bubbles. The transport of lower, denser layers of fluid into the upper layers by the bubble wake can be clearly seen.

The flow pattern inside the bubble is realized by plotting the planar streamlines in a frame of reference moving with the bubbles (figure 7). Figures 7a,b show the streamlines on the $y-x$ plane at $z = z_c$, while figure 7c shows the same on the $y-z$ plane at $x = x_c$, where z_c and x_c are the z and x coordinates of the volumetric centroid of the bubble respectively. The streamlines in the $y-z$ plane show the two major toroidal vortices along with recirculation zones at the top and bottom within the bubble. The secondary vortices rotate in a direction opposite to the primary vortices. The recirculation zones appear in the $y-z$ planes to the right of x_c when the bubble has a positive u-velocity and vice versa. This shows that the flow is highly three-dimensional within the bubble. This asymmetry can also be observed in figure 7a, where the bubble is moving to the right and 7b, where it is moving to the left. The presence of toroidal vortices along with recirculation zones was previously reported by Falconi *et al.* (2016), where they analyzed the flow phenomena in a laminar Taylor bubble flow in square mini-channel. In their study, they analyzed the motion of a slug bubble which is confined in two directions as opposed to confinement in a single direction in our case.
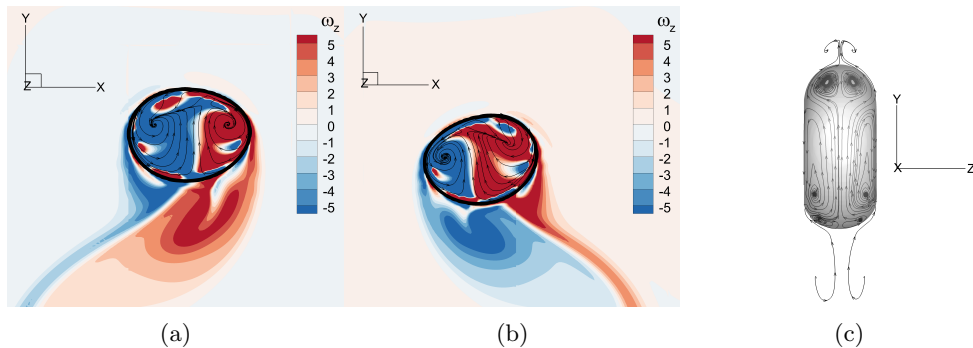
Figure 7: Streamlines within the bubble (a) $y-x$ view at t $= 1.57$s (b) $y-x$ view t=1.79s and (c) $y-z$ view at t $= 1.57$s

4.4. *Rise Velocity*

The slip velocity of the bubble swarm is calculated as

$$v_b(t) = \frac{1}{N_b} \sum_{i=1}^{N_b} v_{b,i}(t) - \frac{1}{V_f} \int_{V_f} v(x, y, z, t) dV, \qquad (4.1)$$

where $v_{b,i}(t)$ stands for the instantaneous vertical velocity of the ith bubble. The second term in equation 4.1 is the volume-averaged velocity of the background fluid, where V_f is the volume of the background fluid and $v(x, y, z, t)$ is the vertical liquid velocity field of the domain. The steady-state average rise velocity of the bubble swarm is obtained by

$$v_{b,avg} = \frac{1}{T - t_0} \int_{t_0}^{T} v_b(t) dt, \qquad (4.2)$$

where the time interval $T - t_0$ is chosen such that the slip velocity of the swarm has crossed the transient stage and is at a statistical steady state.

Figure 8a gives the time variation of Reynolds number of the bubbles for different void fractions at $Fr = 6.37$. We see a slight drop in velocity from $\alpha = 3.35\%$ to $\alpha = 13.4\%$ (a 11% decrease). This is more apparent from the plot of time-averaged Reynolds number against void fraction (figure 8b). Several simulations with slightly different initial conditions are used to calculate the time-averaged bubble rise velocity with error bars corresponding to the lowest and highest average velocity obtained from these simulations. The error bars show that the variations of velocity for different void fractions overlap, and thus we cannot infer a clear trend. In the unconfined case, a steady and more pronounced (a 30% decrease) drop in rising velocity is observed with an increase in void fraction (Riboux *et al.* (2010)). This can be explained by the hindrance effect, where there is a downward liquid velocity between the bubbles, which increases as the void fraction increases. We see in the confined domain that the hindrance effect is counteracted by a phenomenon where the bubbles get caught in the wake of neighboring bubbles and are accelerated. This phenomenon happens because, in a confined domain, the number of degrees of freedom of the bubbles is less than an unconfined case leading to more wake interactions.

Figure 9a gives the time variation of the Reynolds number of the bubbles for different Froude numbers at $\alpha = 3.35\%$. The time-averaged Reynolds number (figure 9b) again does not show a clear trend, and there is almost no change in the fluctuating bubble velocities as the Froude number increases. This is in contrast to the trend observed for
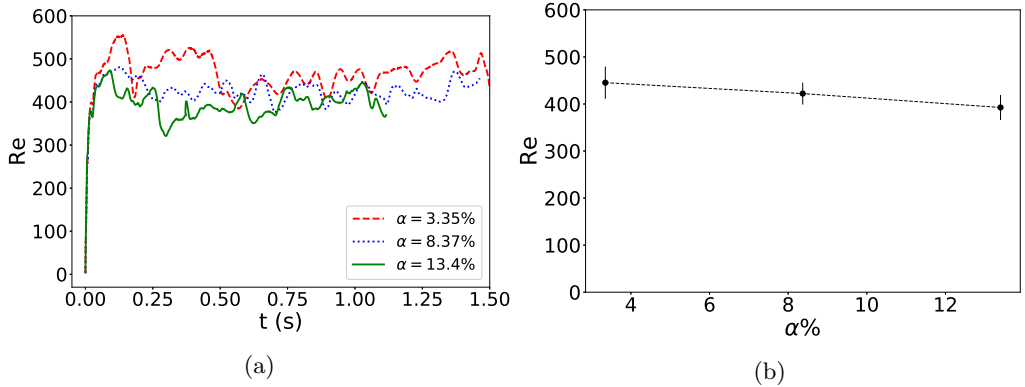
(a)

(b)

Figure 8: Bubble Reynolds number for different void fraction at Fr=6.37 (a)Instantaneous vs time (b)Time averaged vs void fraction
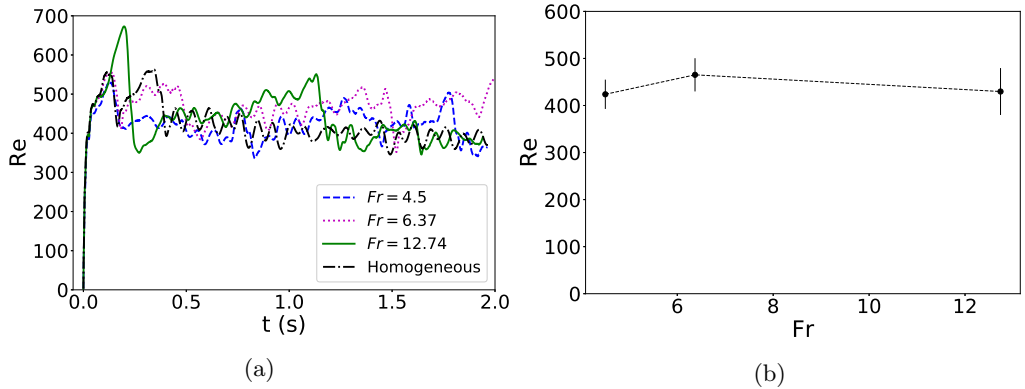

(a)

(b)

Figure 9: Bubble Reynolds number for different Froude numbers at $\alpha = 3.35\%$ (a)Instantaneous vs time (b)Time averaged vs void fraction

drops rising in water Dabiri *et al.* (2015). This is because the density difference between the background fluid and air bubbles is large. The change in density in the fluid created by the stratification is small compared to the density difference between the bubbles and the non-stratified fluid. Since buoyancy force causes the bubbles to rise, the rise velocity of the bubbles does not change significantly with stratification at a constant void fraction.

We see from figure 8a and 9a that the rise velocity shows large fluctuations and drastic dips at isolated times. This happens due to the brief formation of horizontal clusters. Horizontal clusters have been reported in unconfined bubbly flows in homogeneous density fluids (Sangani & Didwania (1993),Yurkovetsky & Brady (1996)) and stratified background fluid (Dabiri *et al.* (2015)). They block the flow and hence cause a drop in the average rise velocity of the bubbles. The velocity dip can happen even when just two bubbles come in close contact in a side-by-side configuration (Bunner & Tryggvason (2002*a*)).

Figure 10a shows the bubble Reynolds number for two different domain sizes $8 \times 16 \times 0.5$ and $16 \times 16 \times 0.5$ (where lengths are non-dimensionalized by $0.625d$). In the second case the domain has been doubled in the horizontal direction, which is the direction in which bubble clusters were observed. This is done in order to see whether the formation of clusters is related to the horizontal size of the periodic domain. The large fluctuations
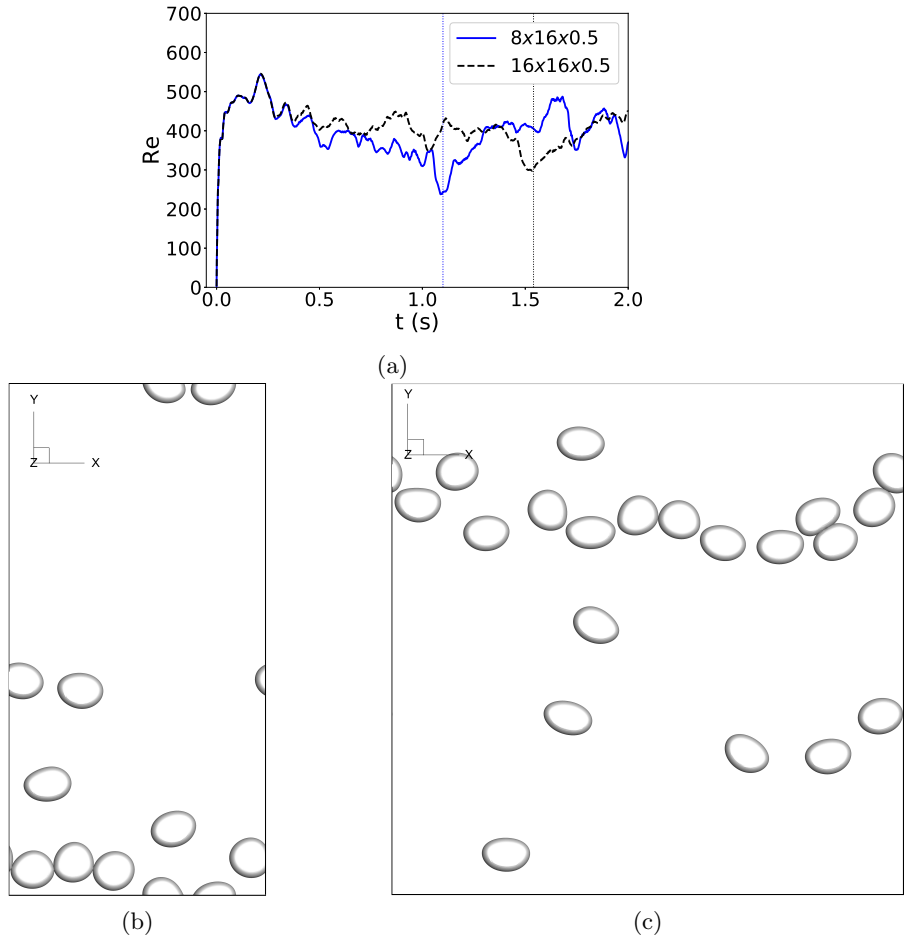
Figure 10: (a) Instantaneous bubble Reynolds number over time for different domain sizes. Cluster Formation shown in (b) 8×16 domain at t = 1.1s and (c) 16×16 domain at t = 1.54s.

and sudden dips in velocity are observed even in the bigger domain. Figure 10b and 10c show the formation of horizontal clusters in both the $8 \times 16 \times 0.5$ and $16 \times 16 \times 0.5$ domains at t = 1.1s and t = 1.54s, respectively. At t = 1.1 s, we see a horizontal cluster in the 8×16 domain in figure 10b and a corresponding dip at 1.1s is observed in the Reynolds number (see figure 10a at the blue dotted line). Similarly, for the 16×16 domain at t = 1.54s, a horizontal cluster (figure 10c) and corresponding velocity dip (see figure 10a at the black dotted line) can be seen.

The formation of horizontal clusters can be quantified by the cluster size index. The marker function is defined as $\phi = 0$ in the dispersed phase and $\phi = 1$ in the continuous liquid phase. We define a cluster size index as follows. Across any horizontal line, the marker function is averaged over the $x - z$ plane, and the minimum through all y locations is taken at each time step. At any time step, a lower value of the cluster size index would imply a higher presence of the gas phase on the horizontal line corresponding to the biggest cluster. This means a larger cluster size. Figure 11 shows a plot of the cluster size index and the corresponding Reynolds number (Re) for different void fractions. We see
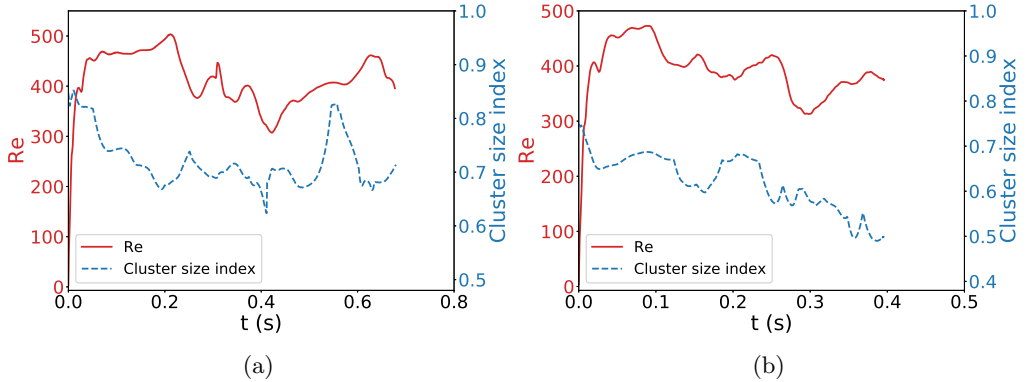
Figure 11: Cluster size index with corresponding Reynolds number for $\alpha =$ (a) 8.37% and (b) 13.4% at Fr=6.37
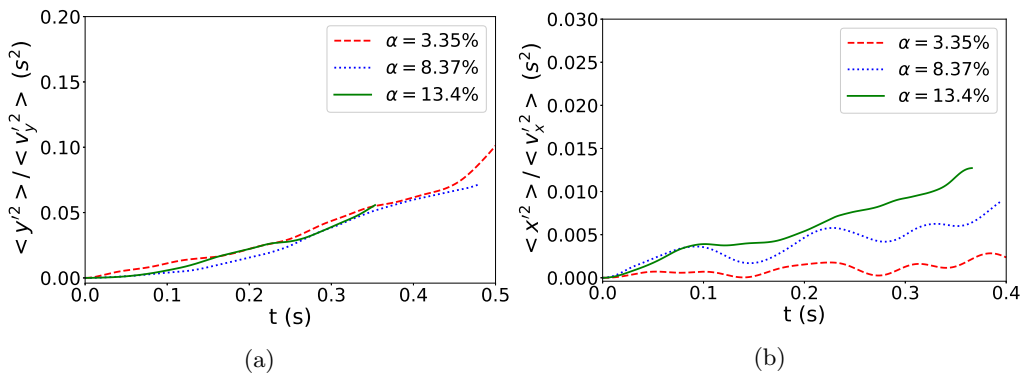

Figure 12: Variance of bubble center displacements with time; (a) and (b) correspond to vertical and horizontal variance at different void fractions at Fr=6.37 respectively

that whenever there is a drop in the cluster size index, there is also a corresponding drop in Re at a slightly later time. This is because the cluster is first formed and then the drop in Re happens (see $t \approx 0.4\text{s}-0.5\text{s}$ in figure 11a and $t \approx 0.1\text{s}-0.2\text{s}$ in figure 11b). A similar cluster formation and immediate breakup have also been observed by Figueroa-Espinoza & Zenit (2005) who studied bubbly flow within a Hele-Shaw cell.

4.5. *Velocity Autocorrelation*

Autocorrelation of horizontal velocity is defined as follows

$$C_{xx}(t) = \frac{\langle v'_{bx}(T)v'_{bx}(T+t)\rangle}{\langle v'^2_{bx}\rangle}, \tag{4.3}$$

where v_{bx} refers to the horizontal bubble velocity, and primed quantities refer to fluctuations. The autocorrelation function determines the behavior of bubbles in the vertical and horizontal directions, gives a measure of whether there are enough bubbles in the domain, and is used to ensure that the statistics calculated are independent of the number of bubbles initialized.

To calculate the autocorrelation function, we need to determine the Lagrangian time scale. To determine this, we look at the bubble center displacements.
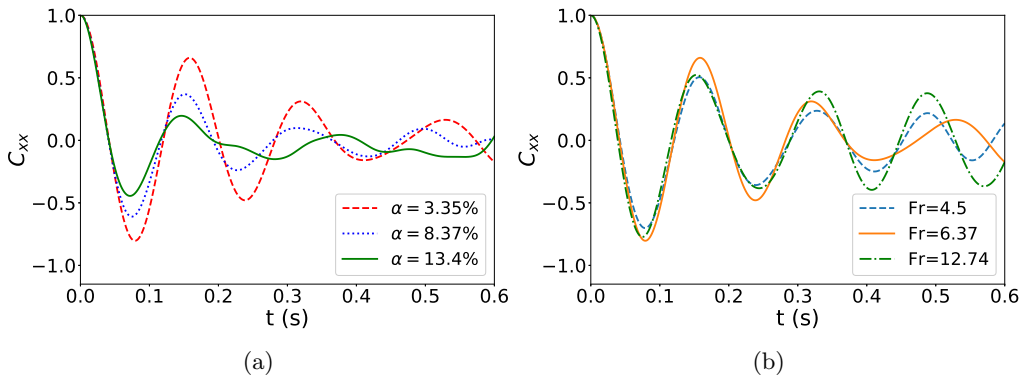
Figure 13: Autocorrelation functions at (a) different void fractions for $Fr = 6.37$ (b) different stratification strengths at $\alpha = 3.35\%$

$$x'(t) = x^{(i)}(t) - \left\langle x^{(i)}(t) \right\rangle, \tag{4.4}$$

where superscript i refers to the ith bubble. From analysis by Taylor (1922) we have

$$\frac{1}{2}\frac{d\left\langle x'^{2}(t)\right\rangle}{dt} = \left\langle v_{bx}'^{2}\right\rangle T_x, \tag{4.5}$$

where $\langle\rangle$ refers to averaging over N_b bubbles, and the variances of bubble center displacements are considered for a significant amount of time. Equation 4.5 is used to find the Lagrangian time scale so that all statistics are calculated for time intervals much greater than T_x.

T_x is thus obtained by plotting $\left\langle x'^{2}(t)\right\rangle$ normalized by $\left\langle v_{bx}'^{2}\right\rangle$ vs time and obtaining the slope of the graph (figure 12). We see that the vertical timescale, calculated to be $T_y = 0.17$s, is approximately the same for different void fractions (figure 12a), a trend also observed by Bouche *et al.* (2012). The horizontal timescale increases as void fraction increases (figure 12b), and at the highest void fraction, we have $T_x = 0.04$s. Similar values for the horizontal and vertical Lagrangian timescale were also obtained by Bouche *et al.* (2012). Bouche *et al.* (2012) have shown that the horizontal Lagrangian integral timescale varies with α as $T_x = 0.33\alpha$s. Thus, for the highest α of 13.4% in our simulations, we have $T_x = 0.045$s, which is very close to the value obtained from our calculations. We also see that the horizontal variance shows oscillations at lower void fractions similar to what was observed by Bouche *et al.* (2012). C_{xx} is obtained for time intervals larger than T_x. We thus plot the horizontal correlations till $t = 0.6$s. Figure 13a shows the plot of C_{xx} for different void fractions. It can be seen that for all void fractions, the autocorrelation function gradually dies down with time, which helps in deducing that the domain size is large enough so that the velocities become uncorrelated after a finite amount of time. The behavior of C_{xx} is also similar to a damped sine wave, which helps to reiterate the fact that the bubbles are moving in a zigzag motion. In fact, in their numerical study of bubbly flow in a Hele-Shaw cell, Wang *et al.* (2014) quantified this horizontal vibration of bubbles using a sine function and investigated the relation between the shape and size of the bubbles and the period of vibration.

It is also seen from figure 13a that, as void fraction increases, the autocorrelation function dies to zero more rapidly. The periodic vortex shedding drives the zigzag bubble path. As void fraction increases, bubbles interact with the wake of neighboring bubbles,

leading to suppression of the orderliness exhibited in the low void fraction region. This, in turn, results in the x-velocities of the bubbles being uncorrelated at a smaller time interval as α increases.

A comparison of C_{xx} for different stratification cases is presented in figure 13b. The time periods of oscillation for all the cases are almost the same with a value of approximately 0.15s. The amplitudes of C_{xx} for the cases also do not vary significantly. This is again attributed to the fact that the density difference between air bubbles and the background liquid is large, because of which the stratification does not have significant effects on the bubble dynamics.

4.6. Mixing

The vortex shedding behind the bubbles, which gives them the zigzag trajectory, also induces mixing in the background fluid. It has been shown in Díaz-Damacillo et al. (2016) that a bubble moving in a zigzag path causes instability and enhances mixing compared to a bubble moving in a rectilinear path. As they move up, the bubbles entrain the background fluid, and the isopycnals get displaced. Once disturbed, the displacement of the isopycnals can be modeled as a damped oscillation with a frequency N, and the time taken for the isopycnals to come back to their stable state is of the order of $1/N$. Mixing occurs when the isopycnals get disturbed repeatedly before they come back to their stable state. Osborn (1980) defined the mixing efficiency and related measurements of energy dissipation to the rate of cross-isopycnal turbulent mixing. In order to quantify the strength of mixing in the background fluid, the following physical parameters are used.

Diapycnal eddy diffusivity gives the vertical mass flux (it represents the cross isopycnal diffusion) and was defined by Osborn (1980) as

$$K_\rho = -\frac{g\overline{\rho'v'}}{\rho_0 N^2}, \tag{4.6}$$

where the overbar represents an ensemble average. This term helps quantify the amount of work done by the buoyancy force.

Cox Number gives the variance of the temperature gradient in the background fluid (Osborn & Cox (1972), Gregg (1977)) and is defined as

$$COX = \frac{\overline{(\nabla T')^2}}{(\partial \overline{T}/\partial y)^2}, \tag{4.7}$$

where $\nabla T'$ gives the gradient of the temperature fluctuation or deviation from the linear temperature distribution, and is normalized by the uniform vertical gradient in the mean temperature imposed due to stratification.

Mixing efficiency gives the ratio of the buoyancy flux to the total energy available for mixing (Briggs et al. (1998), Ivey & Imberger (1991)) and is defined as (Osborn (1980), Shih et al. (2005))

$$\Gamma = \frac{-g\overline{\rho'v'}}{-g\overline{\rho'v'} + 2\mu\overline{E:E}}, \tag{4.8}$$

where E represents the strain rate tensor term. The denominator denotes the sum of the viscous dissipation and the loss to buoyancy. There is viscous dissipation in every direction but a loss to buoyancy only in the vertical component, due to which we have very low values of the mixing efficiency.

Even though we do not have turbulence in our domain, we have velocity fluctuations
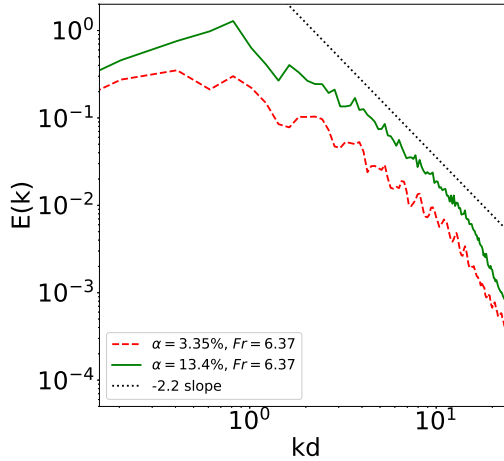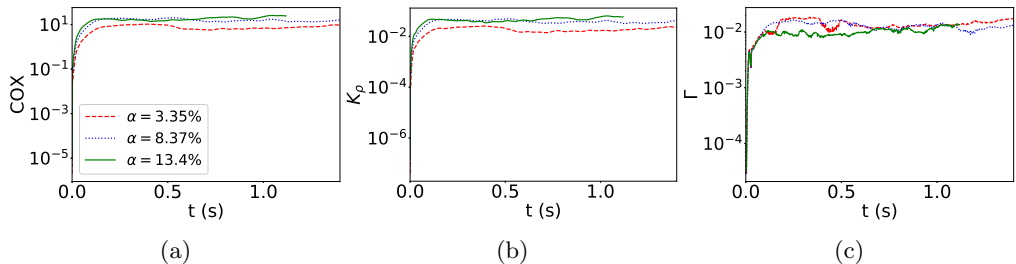
Figure 14: Energy spectrum

Figure 15: Semi-log plot of mixing parameters for varying α at $Fr = 6.37$ (a) COX number (b) Diapycnal eddy diffusivity (non-dimensionalized by $15cm^2/s$) (c) Mixing efficiency

induced by the bubbles. As we have already shown, the motion of the bubbles produces counter-rotating vortices. The bubble wakes also interact with each other. Through the calculation of the diapycnal eddy diffusivity, we are effectively looking at the transport and diffusion of density layers due to bubble induced velocity fluctuations in the background fluid. The capture and transport of fluid in the bubble wake is responsible for the mixing process, and hence looking at these mixing quantities is relevant here. We further look at the energy spectrum in our domain and observe an energy cascade, much similar to turbulent flow (figure 14). The linear slope we obtain is -2.2, which is different from the -5/3 slope in conventional turbulent flows since we have a two-phase flow. Studies in the literature (Bunner & Tryggvason (2002b)) have observed a -3.6 slope for the energy spectrum in unbounded, non-stratified bubbly flows.

4.6.1. *Effect of void fraction*

Figure 15 shows the semi-log plot of mixing parameters as a function of time at different void fractions at a Froude number of 6.37. It can be seen that as the void fraction increases, the COX number and eddy diffusivity increase while mixing efficiency decreases slightly. Thus, it can be concluded that as void fraction increases, the buoyancy flux across the pycnolines increases. However, the viscous dissipation also increases proportionally. The competing effects of the viscous dissipation and the vertical mass flux lead to a
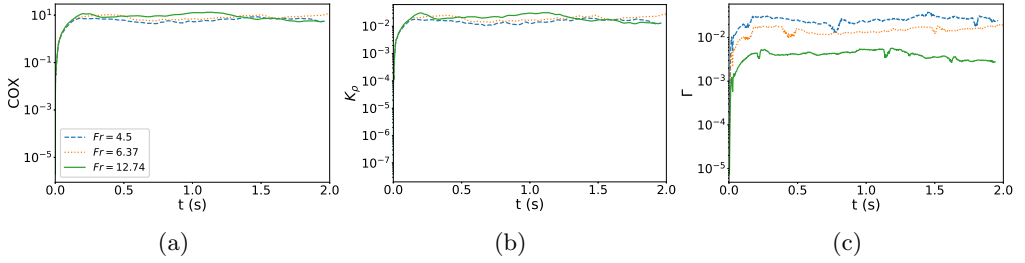
Figure 16: Semi-log plot of mixing parameters for varying Fr at $\alpha = 3.35\%$ (a) COX number (b) Diapycnal eddy diffusivity (non-dimensionalized by $15cm^2/s$) (c) Mixing efficiency

slightly decreasing trend in Γ. Figures 17a-c show the variation of the time-averaged mixing quantities with α for two different Froude numbers. The time averaging is done after omitting the initial transient phase. The trends observed for the COX number and the eddy diffusivity are similar. The change in the mixing efficiency with the void fraction is orders of magnitude less than the change in COX number and eddy diffusivity. The trend in eddy diffusivity, being the measure of cross isopycnal diffusion, can be compared to the diffusion coefficient of a low diffusive dye calculated at different void fractions by Alméras *et al.* (2018). They performed experiments to study the mixing induced by bubbles in a Hele-shaw cell. They reported the existence of asymmetry in the concentration profiles, even though the concentration distribution tends towards a normal distribution. They attributed this to the fact that the mixing mechanism in a two-dimensional column is mainly due to capture and transport by bubble wakes, and turbulent fluctuations are virtually absent. They also observed that an increase in α to 10% resulted in an increase in the diffusion coefficient. Any further increase in α resulted in plateauing of the diffusion coefficient. We also obtain a similar trend in the diapycnal eddy diffusivity where the increase from $\alpha = 3.35\%$ to $\alpha = 8.37\%$ is more pronounced than from $\alpha = 8.37\%$ to $\alpha = 13.4\%$ (see figures 15b and 17a).

4.6.2. *Effect of Froude Number*

Figure 16 shows that, as Froude number increases (i.e., the strength of stratification decreases), mixing efficiency goes down significantly while the COX number and the eddy diffusivity increase. The time-averaged quantities are plotted in figures 17d-f. In this study, the stratification is controlled by the thermal expansion coefficient, γ, while the background temperature gradient is not changed. Since the COX number quantifies the temperature gradient in the liquid, it does not change much with a change in the Froude number when we retain the same initial temperature profile. The only change we see is due to the turbulent transport of temperature due to fluctuations, which increases as we weaken the stratification. In the case of the eddy diffusivity, a change in γ produces a linear change in N^2 and also a linear change in the density perturbation in the background fluid. This leads to an increase in the eddy diffusivity with an increase in Fr. The increase in eddy diffusivity as the strength of the stratification decreases happens because, at high stratifications, the isopycnals come back to their stable state before thermal diffusion can take place. This is because the force pulling the disturbed isopycnal back to its stable state is high, which is also reflected in a high buoyancy frequency. As the strength of stratification decreases, time taken to come back to the original state increases (since the buoyancy frequency is lower), and this facilitates thermal diffusion, enhancing mixing. Since the mixing efficiency increases with an increase in the stratification strength,
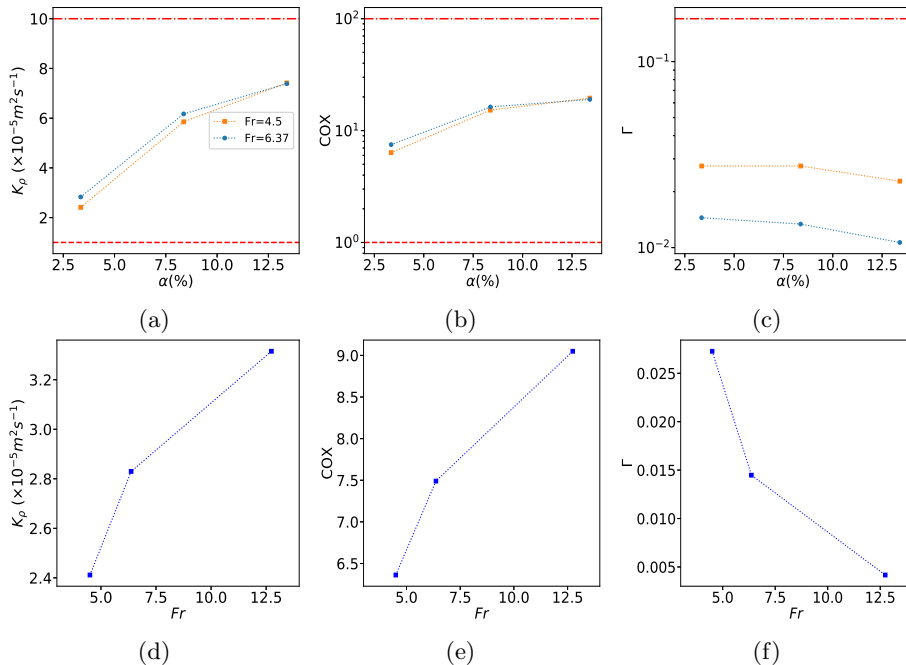
Figure 17: Time averaged (a,d) Diapycnal eddy diffusivity (b,e) COX number (c,f) Mixing efficiency, plotted against α for two different Froude numbers and plotted against Fr for $\alpha = 3.35\%$ respectively. Red $--$ and $-\cdot-$ correspond to lower and upper bounds respectively predicted by Gregg (1977) in (a), Shih *et al.* (2005) in (b) and (c)

it can be inferred that the percentage of the total energy lost to buoyancy increases as stratification increases. In a nearly homogeneous fluid, mixing efficiency is almost zero. This is because the fluctuations mix fluids of the same density (Briggs *et al.* 1998). Even though the vertical mass flux at higher Froude numbers is more leading to more thermal diffusion, the stratification is weak to begin with. Thus, the extent of homogeneity compared to the original state is less, since we start with a more mixed fluid. Mathematically, we can see that the mixing efficiency is governed by the competing effect of the buoyancy flux and the viscous dissipation. Even though the eddy diffusivity is increasing as we weaken the stratification, the buoyancy frequency is decreasing. Since the numerator of Γ is simply $K_\rho N^2$, the competing effects explained previously cancel out. The increase in viscous dissipation is, thus, directly translated into a decrease in Γ.

4.6.3. *Discussion and Scaling*

Eddy diffusivity due to turbulent activities in the ocean was estimated by Moum & Osborn (1986). They observe that for depths ≈ 900m, $K_\rho < 10^{-5}\ m^2s^{-1}$, for depths less than 2000m, $K_\rho < 5 \times 10^{-5}\ m^2s^{-1}$ and the deep estimate for K_ρ approaches a value of $10^{-4}\ m^2s^{-1}$. The lower and upper bounds of the diapycnal eddy diffusivity have been plotted in figure 17a. Similarly, the range of COX numbers in the central North Pacific region were found to vary between 10^0 and 2×10^2 by Gregg (1977). They also found that the most intense activity occurs above and below the main thermocline. Once again, we plot the upper and lower bounds in figure 17b and find that our values lie within these bounds. Mixing efficiency in oceanography is of the order of 0.17-0.2 (Shih *et al.* (2005)). We have plotted the lower bound in figure 17c. Mixing efficiency levels
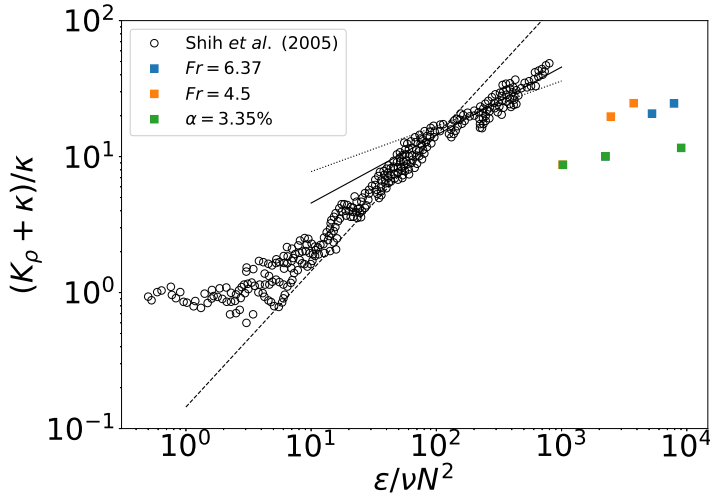
Figure 18: Total scalar diffusivity normalized by molecular diffusivity versus the normalized viscous dissipation. Fit to data taken from Shih *et al.* (2005): $--$, $(K_\rho + \kappa)/\kappa = 0.2Pr\epsilon/\nu N^2$; $\cdots$, $(K_\rho+\kappa)/\kappa = 5Pr(\epsilon/\nu N^2)^{1/3}$; $-$, $(K_\rho+\kappa)/\kappa = 2Pr(\epsilon/\nu N^2)^{1/2}$
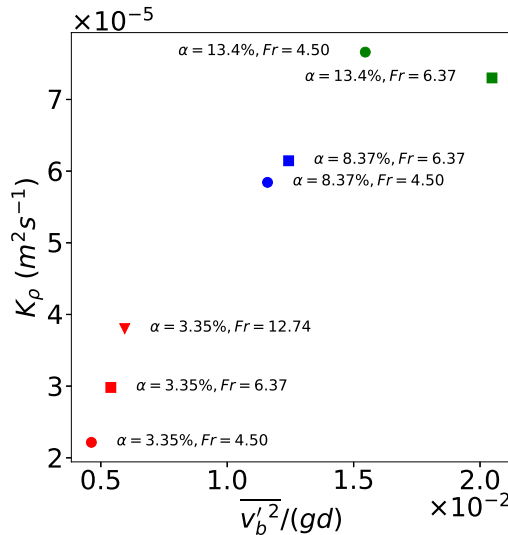

Figure 19: Variation of K_ρ with bubble velocity fluctuations. Same colors correspond to same α. Same shapes correspond to same Fr

present in the ocean scales due to turbulence is not achieved here. The COX number and mixing efficiency variation with α are plotted on a semi-log scale (figure 17b,c) so that the upper and lower bounds can be incorporated in the same plot.

Experiments on stably stratified grid turbulence have suggested that K_ρ can be expressed in terms of $\epsilon/\nu N^2$, where ϵ is the viscous dissipation (Shih *et al.* (2005)). Shih *et al.* (2005) examined these results for homogeneous shear stratified turbulence and find the scaling between K_ρ and $\epsilon/\nu N^2$. They found that the calculated K_ρ values collapsed very well over the entire range of $\epsilon/\nu N^2$. A plot of K_ρ versus $\epsilon/\nu N^2$ is shown in figure 18 where we collapse all our data along with the data from Shih *et al.* (2005). We find

that we are able to achieve similar levels of eddy diffusivity as shear induced turbulence, although it is important to note that we use stronger levels of stratification ($N \approx O(10^0)$). The mixing due to motion of confined bubbles can generate eddy diffusivities as strong as turbulent mixing, but it occurs at much larger values of energy dissipation compared to turbulent mixing. The eddy diffusivity values could be higher for unbounded cases. From figure 18, we can see clearly that the scaling of eddy diffusivity obtained for turbulent mixing is not applicable for our data.

In order to further quantify mixing and how it is affected by the bubble dynamics, we look the scaling of the diapycnal eddy diffusivity with average bubble velocity fluctuations, $v_b'^2$, which is defined as

$$\overline{v_b'^2} = \overline{\left(v_b^{(i)} - \left\langle v_b^{(i)} \right\rangle\right)^2} \tag{4.9}$$

where the overbar refers to averaging over time and also over the bubbles. We collapse all the cases of void fractions and Froude numbers, as shown in figure 19.

We see that as the vertical bubble velocity fluctuations increase, the diapycnal mixing also increases, while at high values of fluctuations, it starts to plateau. Another interesting observation from this figure is that at the two lower void fractions, an increase in Fr leads to an increase in both the bubble fluctuations and the eddy diffusivity. At the highest void fraction, we see that the fluctuation increases with Fr, but K_ρ has attained a plateau. We also see that at a constant Fr, increasing α increases the fluctuation and the mixing monotonically.

5. Conclusion

The bubble dynamics and mixing induced in stratified fluids by the bubble motion in a Hele-Shaw type of cell have been studied. The confinement keeps turbulence at bay, and thus the mixing produced primarily due to transport by the bubble wake is studied. The trends observed in the rise velocity for different void fractions are different in the confined environment compared to the unconfined case. The bubbles are seen to follow a zigzag motion due to the periodic vortex shedding. The zigzag motion has been quantified by looking at the trajectories and autocorrelation of the horizontal bubble velocity. Formation and subsequent breakup of clusters are observed. The size of these clusters has been quantified by the cluster size index, and this index is directly correlated to the instantaneous Reynolds number of the bubbles. An increase in the cluster size results in an instantaneous rise in the bubble Reynolds number. Mixing induced by the bubbles in stratified fluids is quantified through the COX number, diapycnal eddy diffusivity, and mixing efficiency. It is seen that as α increases, the buoyancy flux across the pycnolines also increases, giving rise to a more well-mixed fluid. When the stratification strength is increased, the fraction of total energy lost to buoyancy increases while the cross isopycnal diffusion decreases.

6. Acknowledgement

REFERENCES

ALMÉRAS, E., RISSO, F., ROIG, V., CAZIN, S., PLAIS, C. & AUGIER, F. 2015 Mixing by bubble-induced turbulence. *Journal of Fluid Mechanics* **776**, 458–474.

ALMÉRAS, ELISE, RISSO, FRÉDÉRIC, ROIG, VÉRONIQUE, PLAIS, CÉCILE & AUGIER, FRÉDÉRIC 2018 Mixing mechanism in a two-dimensional bubble column. *Physical Review Fluids* **3** (7), 074307.

ARDEKANI, A. M., DOOSTMOHAMMADI, A. & DESAI, N. 2017 Transport of particles, drops, and small organisms in density stratified fluids. *Physical Review Fluids* **2** (10).

ASAEDA, TAKASHI & IMBERGER, JÖRG 1993 Structure of bubble plumes in linearly stratified environments. *Journal of Fluid Mechanics* **249**, 35–57.

BAINES, W. D. & LEITCH, A. M. 1992 Destruction of Stratification by Bubble Plume. *Journal of Hydraulic Engineering* **118** (4), 559–577.

BAYAREH, M., DABIRI, S. & ARDEKANI, A. M. 2016 Interaction between two drops ascending in a linearly stratified fluid. *European Journal of Mechanics - B/Fluids* **60**, 127–136.

BLANCHETTE, F. 2013 Mixing and convection driven by particles settling in temperature-stratified ambients. *International Journal of Heat and Mass Transfer* **56** (1-2), 732–740.

BOUCHE, E., CAZIN, S., ROIG, V. & RISSO, F. 2013 Mixing in a swarm of bubbles rising in a confined cell measured by mean of PLIF with two different dyes. *Experiments in Fluids* **54** (6).

BOUCHE, E., ROIG, V., RISSO, F. & BILLET, A. 2012 Homogeneous swarm of high-Reynolds-number bubbles rising within a thin gap. part 1. bubble dynamics. *Journal of Fluid Mechanics* **704**, 211–231.

BOUCHE, E., ROIG, V., RISSO, F. & BILLET, A. 2014 Homogeneous swarm of high-Reynolds-number bubbles rising within a thin gap. part 2. liquid dynamics. *Journal of Fluid Mechanics* **758**, 508–521.

BRIGGS, DAVID A, FERZIGER, JOEL H, KOSEFF, JEFFREY R & MONISMITH, STEPHEN G 1998 Turbulent mixing in a shear-free stably stratified two-layer fluid. *Journal of Fluid Mechanics* **354**, 175–208.

BUNNER, B. & TRYGGVASON, G. 2002*a* Dynamics of homogeneous bubbly flows Part 1. Rise velocity and microstructure of the bubbles. *Journal of Fluid Mechanics* **466**.

BUNNER, B. & TRYGGVASON, G. 2002*b* Dynamics of homogeneous bubbly flows Part 2. Velocity fluctuations. *Journal of Fluid Mechanics* **466**.

BUSH, J. W. M. & EAMES, I. 1998 Fluid displacement by high Reynolds number bubble motion in a thin gap. *International Journal of Multiphase Flow* **24** (3), 411–430.

CHEN, M.H. & CARDOSO, S.S.S. 2000 The mixing of liquids by a plume of low-Reynolds number bubbles. *Chemical Engineering Science* **55**, 2585–2594.

CHORIN, A. J. 1968 Numerical solution of the Navier-Stokes equations. *Mathematics of Computation* **22** (104), 745–745.

DABIRI, S. & BHUVANKAR, P. 2016 Scaling law for bubbles rising near vertical walls. *Physics of Fluids* **28** (6), 062101.

DABIRI, S., DOOSTMOHAMMADI, A., BAYAREH, M. & ARDEKANI, A. M. 2015 Rising motion of a swarm of drops in a linearly stratified fluid. *International Journal of Multiphase Flow* **69**, 8–17.

DÍAZ-DAMACILLO, L., RUIZ-ANGULO, A. & ZENIT, R. 2016 Drift by air bubbles crossing an interface of a stratified medium at moderate Reynolds number. *International Journal of Multiphase Flow* **85**, 258–266.

FALCONI, C. J., LEHRENFELD, C., MARSCHALL, H., MEYER, C., ABIEV, R., BOTHE, D., REUSKEN, A., SCHLÜTER, M. & WÖRNER, M. 2016 Numerical and experimental analysis of local flow phenomena in laminar Taylor flow in a square mini-channel. *Physics of Fluids* **28** (1), 012109.

FALGOUT, R. D. & YANG, U. M. 2002 hypre: A Library of High Performance Preconditioners. In *Lecture Notes in Computer Science*, pp. 632–641. Springer Berlin Heidelberg.

FIGUEROA-ESPINOZA, B. & ZENIT, R. 2005 Clustering in high Re monodispersed bubbly flows. *Physics of Fluids* **17** (9), 091701.

GREGG, M. C. 1977 Variations in the Intensity of Small-Scale Mixing in the Main Thermocline. *Journal of Physical Oceanography* **7** (3), 436–454.

IVEY, GN & IMBERGER, J 1991 On the nature of turbulence in a stratified fluid. part i: The energetics of mixing. *Journal of Physical Oceanography* **21** (5), 650–658.

KELLEY, E. & WU, M. 1997 Path Instabilities of Rising Air Bubbles in a Hele-Shaw cell. *Physical Review Letters* **79** (7), 1265–1268.

LEONARD, B. P. 1979 A stable and accurate convective modelling procedure based on quadratic upstream interpolation. *Computer Methods in Applied Mechanics and Engineering* **19** (1), 59–98.

MOUM, JN & OSBORN, TR 1986 Mixing in the main thermocline. *Journal of physical oceanography* **16** (7), 1250–1259.

NETO, I. E. L., CARDOSO, S. S. S. & WOODS, A. W. 2016 On mixing a density interface by a bubble plume. *Journal of Fluid Mechanics* **802**.

OSBORN, T. R. 1980 Estimates of the Local Rate of Vertical Diffusion from Dissipation Measurements. *Journal of Physical Oceanography* **10** (1), 83–89.

OSBORN, T. R. & COX, C. S. 1972 Oceanic fine structure. *Geophysical Fluid Dynamics* **3** (1), 321–345.

RIBOUX, G., RISSO, F. & LEGENDRE, D. 2010 Experimental characterization of the agitation generated by bubbles rising at high Reynolds number. *Journal of Fluid Mechanics* **643**, 509.

RISSO, F. 2018 Agitation, Mixing, and Transfers Induced by Bubbles. *Annual Review of Fluid Mechanics* **50** (1), 25–48.

ROIG, V., ROUDET, M., RISSO, F. & BILLET, A. 2012 Dynamics of a high-Reynolds-number bubble rising within a thin gap. *Journal of Fluid Mechanics* **707**, 444–466.

SANGANI, A. S. & DIDWANIA, A. K. 1993 Dynamic simulations of flows of bubbly liquids at large Reynolds numbers. *Journal of Fluid Mechanics* **250** (-1), 307.

SHIH, L. H., KOSEFF, J. R., IVEY, G. N. & FERZIGER, J. H. 2005 Parameterization of turbulent fluxes and scales using homogeneous sheared stably stratified turbulence simulations. *Journal of Fluid Mechanics* **525**, 193–214.

SPICKA, P., DIAS, M. M. & LOPES, J. C. B. 2001 Gas–liquid flow in a 2D column: Comparison between experimental data and CFD modelling. *Chemical Engineering Science* **56** (21-22), 6367–6383.

TAYLOR, GEOFFREY I 1922 Diffusion by continuous movements. *Proceedings of the london mathematical society* **2** (1), 196–212.

UNVERDI, S. O. & TRYGGVASON, G. 1992 A front-tracking method for viscous, incompressible, multi-fluid flows. *Journal of Computational Physics* **100** (1), 25–37.

WANG, S. & ARDEKANI, A. M. 2015 Biogenic mixing induced by intermediate Reynolds number swimming in stratified fluids. *Scientific Reports* **5** (1).

WANG, X., KLAASEN, B., DEGRÈVE, J., BLANPAIN, B. & VERHAEGHE, F. 2014 Experimental and numerical study of buoyancy-driven single bubble dynamics in a vertical Hele-Shaw cell. *Physics of Fluids* **26** (12), 123303.

WANG, X., KLAASEN, B., DEGRÈVE, J., MAHULKAR, A., HEYNDERICKX, G., REYNIERS, M., BLANPAIN, B. & VERHAEGHE, F. 2016 Volume-of-fluid simulations of bubble dynamics in a vertical Hele-Shaw cell. *Physics of Fluids* **28** (5), 053304.

WILMARTH, T & ISHII, M 1994 Two-phase flow regimes in narrow rectangular vertical and horizontal channels. *International Journal of Heat and Mass Transfer* **37** (12), 1749–1758.

YURKOVETSKY, Y. & BRADY, J. F. 1996 Statistical mechanics of bubbly liquids. *Physics of Fluids* **8** (4), 881–895.